Texture descriptors for robust SAR image segmentation

Andrea Rey[a,b,*] **Juliana Gambini**[c,d] **and Claudio Delrieux**[e,f]

[a]Universidad Tecnológica Nacional, Departamento de Matemática, Facultad Regional Buenos Aires, Buenos Aires, Argentina
[b]Universidad Tecnológica Nacional, Centro de Procesamiento de Señales e Imágenes, Facultad Regional Buenos Aires, Buenos Aires, Argentina
[c]Instituto Tecnológico de Buenos Aires, Departamento de Ingeniería Informatica, Buenos Aires, Argentina
[d]Universidad Nacional de Tres de Febrero, Departamento de Ingeniería en Computación, Pcia. de Buenos Aires, Argentina
[e]Universidad Nacional del Sur, Departamento de Ingeniería Eléctrica y de Computadoras, Baha Blanca, Pcia. de Buenos Aires, Argentina
[f]Consejo Nacional de Investigaciones Científicas y Tácnicas de Argentina-CONICET, Buenos Aires, Argentina

Abstract. SAR (synthetic aperture radar) and PolSAR (polarimetric synthetic aperture radar) images fulfill a fundamental role in Earth observation, due to their advantages over optical images. However, the presence of speckle noise hinders their automatic interpretation and unsupervised use, rendering traditional segmentation tools ineffective. For this reason, advanced image segmentation models are sought to overcome the limitations that make an adequate treatment of speckled images difficult. We propose a procedure for SAR and PolSAR image classification, based on texture descriptors, that combines fractal dimension, a specific probability distribution function, Tsallis entropy, and the entropic index. A vector of local texture features is built using a set of reference regions, then a support vector machine classifier is applied. The proposed algorithm is tested with synthetic and actual monopolarimetric and polarimetric SAR imagery, exhibiting visually remarkable and robust results in coincidence with quantitative quality metrics as accuracy and $F1$-score. © *2021 Society of Photo-Optical Instrumentation Engineers (SPIE)* [DOI: 10.1117/1.JRS.15.046511]

Keywords: SAR imagery; texture features; Tsallis entropy; fractal dimension; image classification.

Paper 210498 received Aug. 10, 2021; accepted for publication Dec. 15, 2021; published online Dec. 28, 2022.

1 Introduction

Synthetic aperture radar (SAR) images, either monopolarimetric or fully polarimetric, are extensively used in remote sensing given their advantages over optical imaging. Among these advantages, we can count their obliviousness with respect to daylight and weather conditions, the extraction of polarimetric information that provides relevant cues about landcover properties or phenomena, and the ability to penetrate the soil or other surfaces and provide indirect relevant measures as moisture, canopy, mineral density, etc.[1] These advantages, together with the evolution and growing effectiveness of the underlying electronics, are enabling the fact that satellite constellations with SAR sensors are increasingly frequent, thus triggering a surge of image availability.

However, the speckle noise phenomenon makes these images hard to handle. Speckle noise is a typical undesirable effect arising in active sensing systems that operate by emitting coherent pulses of energy (light or sound) and record the received backscatter signal.[2] This occurs for example in sonar, ultrasound, and radar systems. The pointwise intensity of the backscatter depends *prima facie* on the physical properties of the target surface. But the local lack of physical

*Address all correspondence to Andrea Rey, arey@frba.utn.edu.ar

1931-3195/2021/$28.00 © 2021 SPIE

coherence in the target may produce self-interference phenomena, which are received at the detector as random pointwise fluctuations in the sensed intensities. A physically encompassing modeling of this phenomenon can be dauntingly complex. Notwithstanding this, adequate and effective models have been proposed, which regard speckle noise as a stochastic, multiplicative variable with a specific statistical distribution. In Refs. 3 and 4, a review of SAR image statistical models that arise from this assumption is provided. Following the multiplicative model, Frery et al.[5] introduced the $\mathcal{G}_I^0$ distribution, which has been used for SAR data analysis because it is a suitable way for modeling areas with different kinds of texture. The $\mathcal{G}_I^0$ distribution is shaped by three parameters: α is related to the target texture, γ is related to the brightness (also called scale parameter), and L is the number of looks, which describes the signal-to-noise ratio. The first two are locally estimated, while the latter is the same for the whole image and can be either known or estimated. Estimations of the α parameter are usually used as an image texture descriptor.

Another approach to describe image textures is by means of fractal features.[6,7] Fractal dimension (FD) characterizes the geometric complexity and the scale invariance properties of a given set.[8] The box-counting technique is widely used for image FD computation, since it exhibits a good tradeoff between precision and computational cost. Another algorithm for image FD estimation is the triangular prism surface area method,[9] where FD is computed by regarding the image as a height field. In this work, both procedures are used to evaluate local texture features.

Besides, information theory provides useful methods to assess and quantify the disorder degree (or entropy) of a dataset, which has been used in many image processing problems, such as segmentation and classification.[10,11] Tsallis entropy was proposed in Ref. 12 as a generalization of Shannon entropy,[13] and the underlying concepts were employed as a texture descriptor for polarimetric synthetic aperture radar (PolSAR) image segmentation.[14]

Inspired by these works, we present a new approach for SAR and PolSAR image classification using a supervised learning algorithm that segments the image by means of texture features. We introduce a local texture feature vector to represent regions with different types of texture, and the support vector machine (SVM) classification method[15] is used, since it requires far less computational power as compared with deep convolutional networks used for SAR image classification.[16–18] Since we are interested in a multiclass-classification, a one-against-one-approach is used. Thus, for h classes, a voting scheme defines the appropriate class after $h(h-1)/2$ binary classifiers are trained.

Our approach is tested with synthetic monopolarimetric SAR data as well as monopolarimetric and polarimetric actual SAR images. The performance is assessed by means of standard metrics, as computed from the confusion matrix. The results show that our approach is suitable for distinguishing regions such as water, pasture, forest, or urban zones according to their texture features.

The main contribution of this article is a feature vector including diverse texture descriptors used to train an SVM methhod for actual SAR image classification. Neither preprocessing nor noise removal methods are applied to the images used for this analysis. The presence of noise is indirectly considered through the texture parameter of the $\mathcal{G}_I^0$ distribution, the FD, the box-counting dimension, and the Tsallis entropy.

The remainder of this paper is organized as follows: the texture descriptors used in this article are introduced in Sec. 2, including $\mathcal{G}_I^0$ distribution parameters, two different methods for FD estimation, the entropic index, and Tsallis entropy computation. Section 3 presents the proposed process for image classification using texture descriptors. In Secs. 4.1 and 4.2, we show the results of applying the proposed segmentation method to synthetic and actual data, respectively, including PolSAR images. In Sec. 5, an overview on the obtained results is presented. Finally, in Sec. 6, we elaborate on the limitations and drawbacks of our contribution and propose future research lines.

2 Texture Descriptors

Texture descriptors are widely used in image classification problems. In Refs. 19 and 20, the authors present a review of texture features and methods for texture recognition, applied to optical images. Speckle noise contamination in general requires different image processing

treatment, and texture descriptors are no exception. For this reason, in this section, we briefly introduce three mathematical formalisms that individually have been used for robust texture descriptors in SAR images, and then we show how they can be combined for image classification. The algorithms for computing texture descriptors are independent of each other. Readers familiar with any of these formalisms can skip the corresponding subsections.

2.1 $\mathcal{G}_I^0$ Distribution

In this work, the $\mathcal{G}_I^0$ distribution is used as a suitable model for image areas with different kinds of textures. This distribution is less computationally complex as compared with other distributions, as the $\mathcal{K}$ or generalized Rayleigh distributions. The $\mathcal{G}_I^0$ distribution does not involve integral functions, for instance, the Bessel function and its parameters have a direct interpretation. This point is extensively analyzed in Ref. 21. Under the multiplicative model, the return $Z = X \cdot Y$ follows a $\mathcal{G}_I^0(z;\alpha,\gamma,L)$ distribution, where X and Y correspond to the backscatter and the speckle noise, respectively. Speckle noise Y follows a $\Gamma(L,L)$ distribution, with probability density function (PDF) given as

$$f_Y(y;L) = \frac{L^L}{\Gamma(L)} y^{L-1} \exp(-Ly). \tag{1}$$

The physics of the image formation imposes $L \geq 1$.

The model for the backscatter X may be any distribution with positive support. One possibility is to use the reciprocal Gamma law, a particular case of the generalized inverse Gaussian distribution, which is characterized by the following PDF:

$$f_X(x;\alpha,\gamma) = \frac{\gamma^{-\alpha}}{\Gamma(-\alpha)} x^{\alpha-1} \exp(-\gamma/x), \tag{2}$$

where $\alpha < 0$ and $\gamma > 0$ are the texture and scale parameters, respectively.

Finally, the return Z can be modeled by $\mathcal{G}_I^0(z;\alpha,\gamma,L)$ whose PDF is

$$f_Z(z) = \frac{L^L \Gamma(L-\alpha)}{\gamma^\alpha \Gamma(-\alpha)\Gamma(L)} \cdot \frac{z^{L-1}}{(\gamma + zL)^{L-\alpha}}, \tag{3}$$

where $-\alpha, \gamma, z > 0$ and $L \geq 1$. The α parameter has noteworthy interpretations related to the roughness of the target. A value of $\alpha \in [-3,0)$ is associated with extremely rough terrains, such as urban zones. Intermediate textured areas such as forests or cultivated zones with high canopy correspond to $\alpha \in [-6,-3)$. Finally, smooth areas such as pastures and flat bare land regions yield an $\alpha \in (-\infty,-6)$.

To estimate the parameters of the $\mathcal{G}_I^0$ distribution, the maximum likelihood (ML) estimation method can be applied as follows. Given $\mathbf{z} = (z_1,\ldots,z_n)$, a sample of independent and identically distributed random variables with common distribution $\mathcal{G}_I^0(z;\alpha,\gamma,L)$ and $(\alpha,\gamma) \in \Theta = \mathbb{R}^- \times \mathbb{R}^+$, an ML estimator of (α,γ) satisfies

$$(\hat{\alpha},\hat{\gamma}) = \arg\max_{(\alpha,\gamma)\in\Theta} \mathcal{L}(\alpha,\gamma,L,\mathbf{z}), \tag{4}$$

where $\mathcal{L}(\alpha,\gamma,L,\mathbf{z}) = \prod_{i=1}^n f_Z(z_i)$ is the likelihood function, and f_Z is given in Eq. (3). This leads to $\hat{\alpha}$ and $\hat{\gamma}$ such that

$$\begin{aligned} n[\Psi^0(-\hat{\alpha}) - \Psi^0(1-\hat{\alpha})] + \sum_{i=1}^n \ln\left(\frac{\hat{\gamma} + Lz_i^2}{\hat{\gamma}}\right) &= 0, \\ \frac{n\hat{\alpha}}{\hat{\gamma}} - (L-\hat{\alpha}) \sum_{i=1}^n \frac{1}{\hat{\gamma} + Lz_i^2} &= 0, \end{aligned} \tag{5}$$

where $\Psi^0(t) = d\ln\Gamma(t)/dt$ is the digamma function. This system can be solved with the BFGS[22] method, but given that the likelihood function $\mathcal{L}(\alpha,\gamma,L,\mathbf{z})$ is flat, its maximization leads to many numerical problems, which are discussed in Ref. 23.

2.2 *Fractal Dimension Estimation*

Let $U \subset \mathbb{R}^n$ be a nonempty set and define $|U| = \sup\{\|x - y\| : x, y \in U\}$ its diameter. Denote with $\{U_i\}_{i\in I}$ a countable class of sets in $\mathbb{R}^n$ such that for every $i \in I$ it holds that $\sup\{|U_i|\} \leq r$. Then, for every $F \subseteq \cup_{i\in I} U_i$, $\{U_i\}_{i\in I}$ is an r-cover of F. Consider a closed set $A \subset \mathbb{R}^n$ and let $N_r(A)$ be the smallest number of sets with diameter at most r that cover A. Then, the box-counting dimension of A is given as

$$\mathrm{BC} = \lim_{r\to 0} \frac{\log(N_r(A))}{\log(1/r)}, \tag{6}$$

if the limit exists and it is used as an FD estimation of the set A. If A is a planar set, squared cells of side r can be used and its box-counting dimension is related to the number of cells where the set has non-null measure. The process for numerically calculating BC of a binary image consists of partitioning the image in squared cells of side r and averaging the number of cells N_r required to cover A. This is performed for several values of r. Finally, BC can be estimated as the slope of the regression line that fits the points $(\log(N_r), \log(1/r))$. Real-valued images require to be binarized before computing BC.

Another method, suitable for the FD estimation of images, regards the image as a topographic surface.[9] This algorithm is a two-dimensional generalization of the "walking dividers" used to evaluate the FD of linear features (e.g., coastal lines). In this method, the image is considered as a height field, whose surface is divided into cells of size $r \times r$. Each cell is partitioned into four triangles (using its center as a common vertex). The following step is to calculate the areas of the tops of the prisms that result from vertically projecting these triangles to their given heights. This process is repeated varying the cell size. Smaller cell sizes catch more detail of the height field. If β is the slope of the linear fitting of the total area as a function of the cell size in log–log space, then the FD is estimated as

$$\widehat{\mathrm{FD}} = 2 - \beta. \tag{7}$$

Since β can be regarded as a self correlation parameter,[24] enhanced self-correlation estimation methods can achieve more robust FD evaluation results.[25]

2.3 *Entropy*

Entropy is a fundamental concept related to the notion of disorder in statistics. Given $p(x;\theta)$ a PDF in a space Ω, where $\theta = (\theta_1, \ldots, \theta_r)$ is a parameter vector in the parameter space Θ, and a sample $\mathbf{z} = (z_1, \ldots, z_n)$, the standard expression of the entropy of the sample, following Shannon,[13] is given as

$$S(\theta) = -\sum_{i=1}^{n} p(z_i, \theta) \ln(p(z_i;\theta)). \tag{8}$$

Tsallis proposed in Refs. 12 and 26 a generalization of the Shannon entropy is given as

$$S_T(\theta) = \frac{1}{q-1}\left(1 - \sum_{i=1}^{n} p(z_i, \theta)^q\right), \tag{9}$$

where $q \in \mathbb{R}$. When $q \to 1$ in Eq. (9), $S_T(\theta)$ tends to $S(\theta)$, Eq. (8), and thus q, as a generalization parameter is called entropic index, and is a free parameter that characterizes the nonextensivity degree of the model. When $q > 1$, the model provides a higher weight to the inliers in $p(z_i;\theta)$, and the opposite is the case when $q < 1$. In this work, we compute the entropic index using the method proposed in Ref. 27 because it has been successfully used in optical image segmentation by considering the q value that maximizes the redundancy as an image feature. Algorithm 1 shows the process to compute the q value for a given image.

Algorithm 1 Optimum Tsallis entropic index computation algorithm.

input: Original image *Img*, $a, b \in \mathbb{R} - \{1\}$, $a < b$

output: optimum entropic index q_T

begin

$h \leftarrow$ normalized histogram of *Img*

$p \leftarrow$ nonvanishing values of h

$N \leftarrow$ length of p

for $q \in \{a, a + 0.1, \ldots, b\}, q \neq 1$ **do**

$S_T(q) \leftarrow$ Tsallis entropy

$S_{\max}(q) \leftarrow (1 - N^{1-q})/(q - 1)$ (maximum entropy)

$R_T(q) \leftarrow 1 - S_T(q)/S_{\max}(q)$ (redundancy)

$q_T \leftarrow \underset{q \in \{a, a+0.1, \ldots, b\}}{\arg\max} R_T(q)$

3 SAR Image Classification

In this section, the proposed process for image classification using texture descriptors is presented. The underlying mechanism is to combine together all these textural features, taking advantage of the different information aspects that each one provides. A sliding window of size $s \times s$ is considered to estimate the following texture metrics for each image pixel:

1. ML estimation of the texture parameter $\hat{\alpha}$ of the $\mathcal{G}_I^0$ distribution, using Eq. (5).
2. Box-counting BC computation, using Eq. (6).
3. FD approximation $\widehat{\text{FD}}$, using Eq. (7).
4. Optimum Tsallis entropic index q_T calculated using Algorithm 1.
5. Tsallis entropy S_T, computed with the optimum entropic index described in item 4.

The selection of the sliding window size must be based on a balance between results quality and computational cost. If this size is small, the estimations of entropy, α parameter of the $\mathcal{G}_I^0$ distribution, and FD may be unrepresentative of the region roughness. On the other hand, large window sizes imply a high computational cost with no substantial gain in the quality of the results. Initially, it is possible to investigate SAR image classification properties using all these texture features combined in different ways. In this work, we focus on the following two sets of features: $A^* = \{\hat{\alpha}, \text{BC}, \widehat{\text{FD}}, q_T, S_T\}$ and $A = \{\text{BC}, \widehat{\text{FD}}, q_T, S_T\}$. The set A^* involves the five features introduced above, which take into account different textural aspects. However, the estimation of the α parameter of the $\mathcal{G}_I^0$ distribution requires the numerical maximization of a flat function (with very low derivative), implying a high computational cost. Using the feature set A (i.e., dropping the α parameter estimation), this problem is removed with very little impact on the final results. Then, we apply the SVM model to obtain the classifiers SMV_{A^*} and SMV_A, respectively. The training procedure is performed using labeled patches of the original image. In synthetic images, the region labels are set according to α parameter values used in the image generation, whereas in actual SAR images it is performed by a photointerpretation expert. The regions of interest (RoI) are randomly split according to the usual proportions $60\% - 20\% - 20\%$, the former two for K-fold cross-validation, $K \in \mathbb{N}$, to find the best hyperparameters and the best kernel of the SVM method, and the remaining unseen 20% for testing the model, for more information about validation methods see Ref. 28. In the process of kernel and hyperparameter analysis, the following indicators are computed in every fold: $F1$-score, intersection over union (IoU), and the area under the receiver operating characteristic curve (AUC). Then, the parameters and kernel selection are performed from the best mean and standard deviation of these measures.

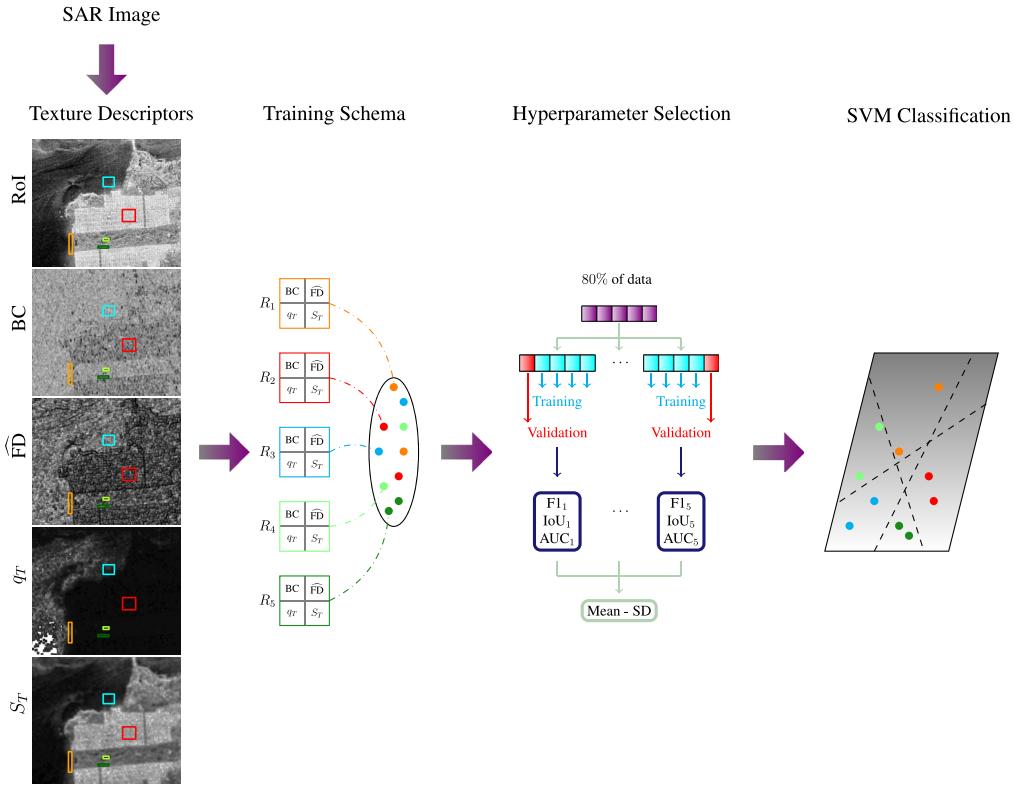

Fig. 1 Schematic representation of the processing workflow of the proposed SAR image classification approach.

Figure 1 shows a scheme of the proposed SAR image classification process. Given the original image, the first column shows the labeled RoI for training in the different texture feature images. The second column represents the SVM model training. The third column summarizes the evaluation of the method using different standard metrics, which are utilized to find the better parameters. The fourth column represents the final multiclass classification.

4 Results

4.1 *Synthetic Image Classification*

In this section, we present the results of applying the proposed SAR image classification method to images generated by plane model with and without outliers. Since we are interested in presenting a new approach that can be used for any type of SAR images, we evaluate our proposal considering different numbers of looks.

4.1.1 *Plain synthetic model*

Following the recommendations proposed in Ref. 29, a synthetic image of size 500×500 is generated using the $\mathcal{G}_I^0$ distribution with parameters $(\alpha, \gamma) \in \{(-6.5, 0.1), (-3.5, 0.1), (-2, 0.1)\}$, $L \in \{1,2\}$, divided into three regions. Figure 2 shows singlelook [Fig. 2(a)] and multilook [Fig. 2(b)] cases, and pixel labels of the synthetic image [Fig. 2(c)], according to high (red), medium (green), and low (blue) textured areas. To compute the feature values for each pixel, we use a sliding window of size $s = 11$, and set $a = -2$ and $b = 8$ the parameters in Algorithm 1. The input parameter values used in the algorithm are empirically selected. For each region, we consider a random training sample of 900 pixels that are at least five pixels apart from the region boundaries.

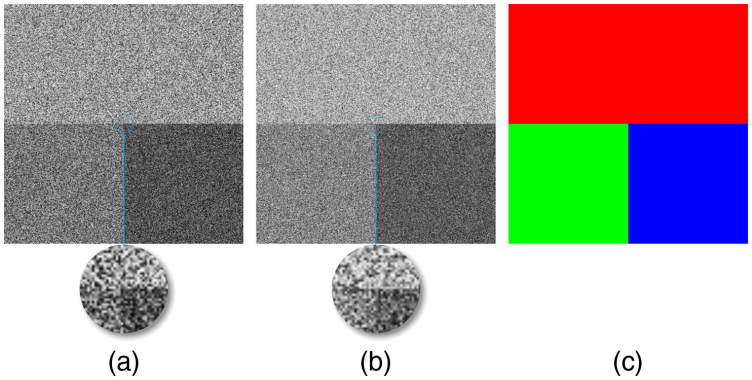

Fig. 2 Synthetic SAR images with (a) $L = 1$ and (b) $L = 2$, with an inset to better visualize the textures. (c) Pixel labels according to high (red), medium (green), and low (blue) textured areas.

An SVM classifier is trained to find optimal values for the cost of constraints violation c, and parameters d and g used in the following kernel functions:

$$\mathrm{Ker}(x,y) = \begin{cases} x \cdot y & \text{linear}, \\ (x \cdot y)^d & \text{polynomial}, \\ \exp(-g\|x-y\|) & \text{radial}, \\ \tanh(gx \cdot y) & \text{sigmoid}. \end{cases} \tag{10}$$

For each kernel, we consider the following hyperparameter values: $c \in \{0.001, 0.01, 0.1, 1{,}5, 10\}$, $d \in \{2{,}3, 4\}$, and $g \in \{0.01, 0.1, 1, 1.5, 2\}$. Thus, to assess the performance of each classifier, in the K-fold cross-validation process with $K = 5$, we compute the mean and standard deviation of the $F1$-score, IoU, and AUC. Using the test set, we compute the accuracy of the best performing model. Table 1 presents the obtained results where the best values are in bold. In the remaining of this section, we restrict the study to the application of both methods as follows:

- Singlelook case: radial kernel; $c = 5$, $g = 0.1$ for SVM_{A^*}; and $c = 1$, $g = 0.01$ for SVM_{A}.
- Multilook case: linear kernel, and $c = 1$.

If several models achieve the same results, we select the simplest. It is remarkable that the α parameter of the $\mathcal{G}_I^0$ distribution as a feature is detrimental or it does not influence the performance of these classifiers. Thus, the costly and numerically error-prone optimization associated with the estimation of this parameter is not required.

Figure 3 shows the results of applying the best classification methods to the images of Fig. 2. Table 2 shows the corresponding confusion matrices. Misclassified pixels, in both models, represent the 0.28% in the singlelook case and only the 0.04% in the multilook case.

4.1.2 *Elaborate synthetic model*

The robustness of an image classification method is related to the ability to perform adequately even when data are noisy or away from the initial assumptions. Since supervised image classification is based on training samples, the incidence of noise in the quality of the resulting model has to be evaluated. In Refs. 30 and 31, this issue is addressed. A commonly occurring situation in actual SAR imagery is the double bounce phenomenon, by which some pixels have an unusual high return value.[2] This causes actual SAR images to contain outliers. To emulate this phenomenon in synthetic images and to further assess the robustness of the models trained in the previous subsection, we use three different types of noise contamination. The underlying idea considers sample data away from the distribution $\mathcal{G}_I^0(z;\alpha,\gamma,L)$ discussed above.

The first type of noise contamination considers that, with probability ε, the observed data have a $\mathcal{G}_I^0$ distribution with parameters that differ from the theoretical ones. The second type

Table 1 Classifier performance assessment and hyperparameter values. Kernel (Ker) are linear (L), polynomial (P), radial (R), or sigmoid (S).

Ker	Parameters	$F1$ mean	$F1$ SD	IoU mean	IoU SD	AUC Mean	AUC SD	Accuracy
(a) Model SVM_{A^*}, $L = 1$								
L	$c = 1$	0.9963	0.0035	0.9926	0.0070	0.9982	0.0018	0.9963
P	$c = 5$, $d = 2$	0.9948	**0.0030**	0.9897	**0.0060**	0.9961	0.0027	0.9870
R	$c = 5$, $g = 0.1$	**0.9967**	0.0031	**0.9935**	0.0062	**0.9984**	0.0016	**0.9926**
S	$c = 1$, $g = 0.01$	0.9958	0.0031	0.9917	0.0061	0.9979	**0.0015**	**0.9926**
(b) Model SVM_A, $L = 1$								
L	$c = 0.01$	0.9967	0.0031	0.9935	0.0062	0.9984	0.0016	**0.9907**
P	$c = 5$, $d = 3$	0.9967	0.0027	0.9935	0.0053	0.9984	**0.0012**	0.9852
R	$c = 1$, $g = 0.01$	**0.9972**	**0.0026**	**0.9944**	**0.0051**	**0.9986**	0.0013	**0.9907**
S	$c = 1$, $g = 0.01$	0.9967	0.0031	0.9935	0.0062	0.9984	0.0016	0.9926
(c) Model SVM_{A^*}, $L = 2$								
L	$c = 1$	**0.9995**	**0.0011**	**0.9991**	**0.0021**	**0.9998**	**0.0005**	**1.0000**
P	$c = 0.1$, $d = 2$	**0.9995**	**0.0011**	**0.9991**	**0.0021**	**0.9998**	0.0006	0.9981
R	$c = 1$, $g = 0.1$	**0.9995**	**0.0011**	**0.9991**	**0.0021**	**0.9998**	**0.0005**	**1.0000**
S	$c = 5$, $g = 0.01$	**0.9995**	**0.0011**	**0.9991**	**0.0021**	**0.9998**	**0.0005**	**1.0000**
(d) Model SVM_A, $L = 2$								
L	$c = 1$	**0.9995**	**0.0011**	**0.9991**	**0.0021**	**0.9998**	**0.0005**	**1.0000**
P	$c = 1$, $d = 2$	0.9991	0.0021	0.9981	0.0042	0.9995	0.0011	0.9981
R	$c = 1$, $g = 0.1$	**0.9995**	**0.0011**	**0.9991**	**0.0021**	**0.9998**	**0.0005**	**1.0000**
S	$c = 5$, $g = 0.01$	**0.9995**	**0.0011**	**0.9991**	**0.0021**	**0.9998**	**0.0005**	**1.0000**

Note: The bold type is used to show the best results.

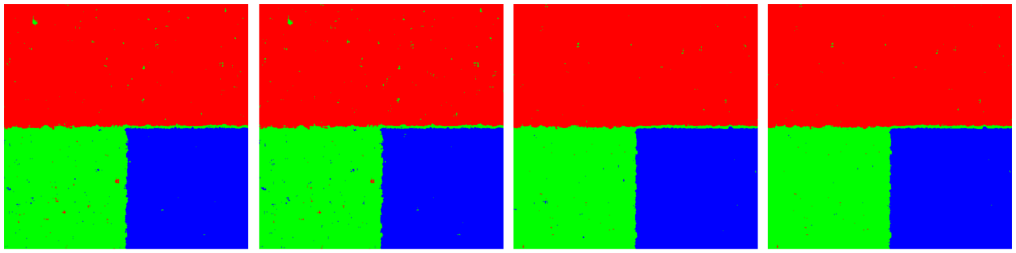

Fig. 3 Synthetic image classification. (a) SVM_{A^*} applied to the singlelook case with 98.78% accuracy. (b) SVM_A applied to the singlelook case with 98.67% accuracy. (c) SVM_{A^*} applied to the multilook case with 99.07% accuracy. (d) SVM_A applied to the singlelook case with 99.10% accuracy.

returns a fixed value $C \in \mathbb{R}^+$, usually large, with probability ε. The third type assumes that the scale parameter value is 10^k larger than the theoretical one. Explicitly, let W be a given region in the synthetic image, generated under $\mathcal{G}_I^0(z; \alpha, \gamma, L)$ distribution, $0 < \varepsilon \ll 1$ is the proportion of noise contamination, and assume B is a Bernoulli random variable with parameter ε. Now the

Table 2 Confusion matrices corresponding to the classifiers applied to the synthetic images. Classes are identified as their corresponding degree of texture.

	Reference		
Prediction	Low	Medium	High
(a) SVM_{A^*} ($L = 1$)			
Low	98.13	0.46	0.00
Medium	1.87	98.70	0.86
High	0.00	0.84	99.14
(b) SVM_A ($L = 1$)			
Low	98.09	0.61	0.00
Medium	1.91	98.69	1.06
High	0.00	0.70	98.94
(c) SVM_{A^*} ($L = 2$)			
Low	98.25	0.24	0.00
Medium	1.75	99.18	0.57
High	0.00	0.58	99.43
(d) SVM_A ($L = 2$)			
Low	98.26	0.15	0.00
Medium	1.74	99.27	0.57
High	0.00	0.58	99.43

model for synthetic region generation will be a convex function $Z = BU + (1 - B)W$ in which we consider the following types U of noise contamination:

- Type I: $U \sim \mathcal{G}_I^0(z; \alpha', \gamma', L)$, $(\alpha', \gamma') \neq (\alpha, \gamma)$.
- Type II: $U = C$.
- Type III: $U \sim \mathcal{G}_I^0(z; \alpha, 10^k\gamma, L)$.

For these experiments, we establish $\varepsilon = 0.1$, $L \in \{1,2\}$, and analyze the noise contaminated images in the following cases: $\gamma' = 0.1$, $\alpha' \in \{-8, -4, -1.5\}$, $C \in \{10^2, 10^3, 10^4\}$, and $k \in \{1,2,3\}$. We apply SVM_{A^*} and SVM_A classification methods to the noise contaminated data, with the same hyperparameters and training set as described in the previous section. The accuracy values of the classifiers applied to the complete image after noise contamination are presented in Table 3.

Figure 4 shows the best and worst results obtained applying the classifier SVM_A^* to two singlelook images under this noise model. Figure 4(a) represents one among the best performances, achieved under type I noise, with $\alpha' = -4$, whereas Fig. 4(b) represents one among the worst classifications, performed under type III noise, with $k = 3$.

4.2 *Actual SAR Image Classification*

In this section, we present the outcomes of the proposed model, applied to classify actual images, in raw format, both monopolarimetric and full polarimetric SAR data. We compare our results with the SNAP suite (version 8.0.8.), which follows a common architecture for the European Space Agency Toolboxes (available at Ref. 32). From this tool, we evaluated the following supervised classifiers: random forest (RF), KDTree KNN (KD), ML, and minimum distance (MD).

Table 3 Accuracy (in percentage) of the classifiers applied to contaminated data.

Noise contamination	SVM_{A^*} ($L = 1$)	SVM_A ($L = 1$)	SVM_{A^*} ($L = 2$)	SVM_A ($L = 2$)
Type I: $\alpha' = -1.5$	**91.47**	90.84	87.01	**87.07**
Type I: $\alpha' = -4$	**98.07**	97.79	96.86	**96.94**
Type I: $\alpha' = -8$	**97.18**	96.61	**96.47**	96.28
Type II: $C = 100$	85.89	**92.97**	93.92	**94.09**
Type II: $C = 1000$	85.82	**92.96**	93.93	**94.08**
Type II: $C = 10{,}000$	85.81	**92.96**	93.94	**94.08**
Type III: $k = 1$	**80.36**	80.25	76.69	**77.62**
Type III: $k = 2$	65.35	**66.05**	65.68	**66.45**
Type III: $k = 3$	64.17	**64.91**	64.73	**65.49**

Note: The bold type is used to show the best results.

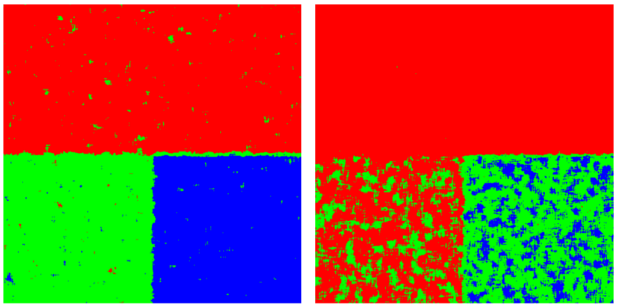

(a) (b)

Fig. 4 Noisy synthetic image classification. (a) Type I noise with $\alpha' = -4$ and $L = 1$. The SVM_{A^*} classifier obtains an accuracy of 98.07%. (b) Type noise III with $k = 3$ and $L = 1$. The SVM_{A^*} classifier obtains an accuracy of 64.17%.

4.2.1 *Monopolarimetric images*

We consider a 2143 × 1146 SAR L-band image taken around the Monte Hermoso city in Buenos Aires Province, Argentina [see Fig. 5(a)], central latitude: 38°57′60″S, central longitude: 61°19′49″W, which is freely available in Ref. 33. Different landcovers can be observed including the Sauce Grande forests, lagoon, sea, sandbanks, and urban. The estimated equivalent number

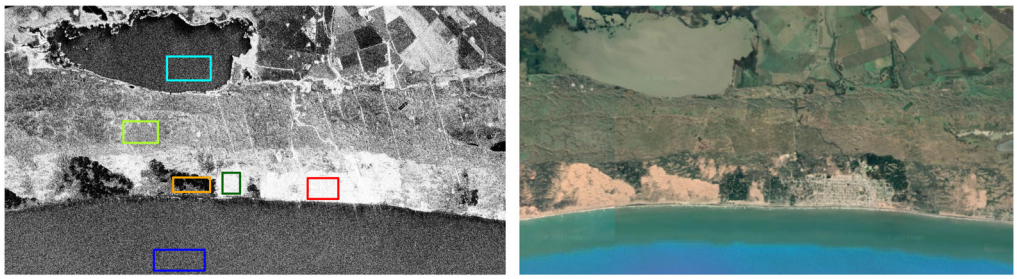

(a) (b)

Fig. 5 SAR image around Monte Hermoso city, Buenos Aires Province, Argentina. (a) The training samples are from urban area (red), lagoon area (cyan), pastures area (light green), sandbank area (orange), sea area (blue), and forest area (dark green). (b) The corresponding optical image from Google Earth.

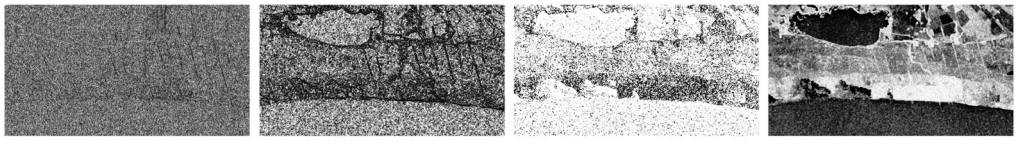

(a) (b) (c) (d)

Fig. 6 Feature maps computed for the image of Fig. 5. (a) $\widehat{\mathrm{FD}}$, (b) $\widehat{\mathrm{FD}}$, (c) q_T, and (d) S_T.

of looks, computed as the quotient between the squared mean and the variance of the sample, is ENL $= 11$. The same area was taken from the optical sensor used by Google Earth [see Fig. 5(b) to facilitate a visual interpretation]. In this latter image, a photo interpretation expert labeled the following reference samples represented as color rectangles in Fig. 5(a): urban area (red, 11,880 pixel), lagoon (cyan, 19,364 pixel), pastures (light green, 13,857 pixel), sandbank (orange, 10,017 pixel), sea (blue, 19,620 pixel), and forest area (dark green, 6840 pixel).

As mentioned above, an accurate estimation of the α parameter of the $\mathcal{G}_I^0$ distribution using actual imagery data requires excessive computation effort, is error-prone, and adds little to the overall classifier performance. For this reason, and motivated by the results obtained with the synthetic images, we focused on the SVM$_A$ method. Figure 6 shows the feature maps computed using a sliding window of size $s = 11$. Figures 6(a)–6(d) correspond to the evaluation of box counting dimension, estimation of FD, optimal entropic index, and Tsallis entropy, respectively. During training, we randomly selected 1000 windows within each labeled region. Then, these sets were randomly partitioned in training (80%) and validation (20%) sets. We applied K-fold cross-validation, with $K = 5$ and computed the mean and standard deviation of $F1$-scores, IoU, and AUC for each fold, Table 4 shows the obtained results. The radial kernel performed best, hyperparameters $c = 10$ and $g = 0.1$, with which we classified the entire image.

To reduce overclassification, a majority filter with a sliding window of size 7×7 is applied. The window size is empirically selected. The results are shown in Fig. 7. In Table 5, we present the resulting confusion matrix. The accuracy values per class as compared with some of the classifiers results by SNAP are shown in Table 6. Figure 8 shows the results of applying RF method [Fig. 8(a)], KD method [Fig. 8(b)], ML method [Fig. 8(c)], and MD method [Fig. 8(d)].

Table 4 SVM$_A$ model performance assessment measures, applied to the image of Fig. 5(a).

Ker	Parameters	$F1$ mean	F1 SD	IoU mean	IoU SD	AUC mean	AUC SD	Accuracy
L	$c = 5$	0.7527	0.0165	0.6191	0.0220	0.7949	0.0176	0.7525
P	$c = 1$, $d = 3$	0.7777	0.0096	0.6458	0.0124	0.8021	0.0104	0.7108
R	$c = 10$, $g = 0.1$	**0.7791**	0.0127	**0.6486**	0.0172	**0.8040**	0.0153	**0.7642**
S	$c = 10$, $g = 0.01$	0.7377	**0.0087**	0.6010	**0.0117**	0.7814	**0.0076**	0.7350

Note: The bold type is used to show the best results.

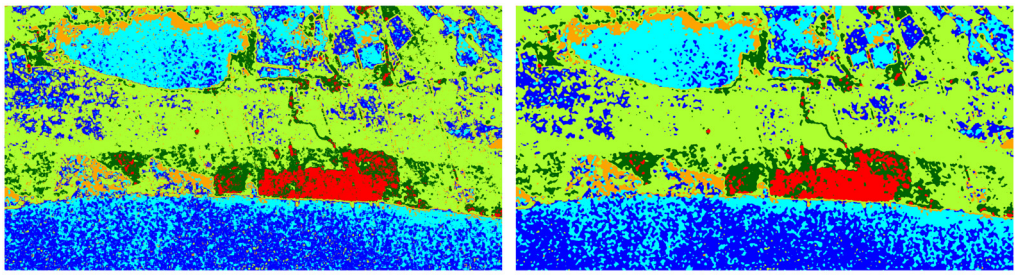

(a) (b)

Fig. 7 (a) Result of applying SVM$_A$ classification method to the image of Fig. 5(a). (b) Result after applying majority filter.

Table 5 Confusion matrices (in percentage) for SVM_A applied to the image of Fig. 5(a) before and after applying majority filter.

	Reference					
Prediction	City	Forest	Lagoon	Pasture	Sandbank	Sea
Before						
City	89.60	22.69	0.00	0.01	0.00	0.00
Forest	10.40	75.96	0.00	0.61	0.08	0.00
Lagoon	0.00	0.00	74.33	0.00	12.91	22.41
Pasture	0.00	1.32	0.01	95.78	12.85	0.94
Sandbank	0.00	0.03	1.22	1.20	57.90	1.08
Sea	0.00	0.00	24.44	2.40	16.26	75.57
After						
City	93.93	18.67	0.00	0.00	0.00	0.00
Forest	6.07	80.73	0.00	0.38	0.00	0.00
Lagoon	0.00	0.00	79.27	0.00	9.76	17.94
Pasture	0.00	0.60	0.00	99.00	12.70	0.02
Sandbank	0.00	0.00	0.01	0.07	60.54	0.44
Sea	0.00	0.00	20.72	0.56	17.00	81.61

Table 6 Comparison of different classifiers applied to image from Fig. 5(a) in terms of accuracy values per class (in percentage).

Classifier	City	Forest	Lagoon	Pasture	Sandbank	Sea
Our proposal SVM_A	**89.52**	75.63	74.31	**95.82**	57.72	75.55
RF	85.51	81.69	77.57	79.39	84.93	77.29
KD	86.45	82.09	76.31	79.15	87.71	**79.59**
ML	88.09	83.69	76.75	82.21	**89.91**	78.85
MD	88.43	**84.03**	**81.65**	81.19	82.99	79.25

Note: The bold type is used to show the best results.

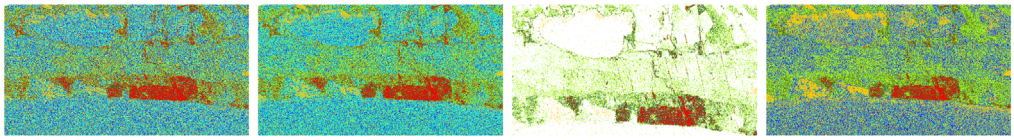

(a) (b) (c) (d)

Fig. 8 Results of applying different classifiers to the image of Fig. 5(a). (a) RF. (b) KD. (c) ML. (d) MD.

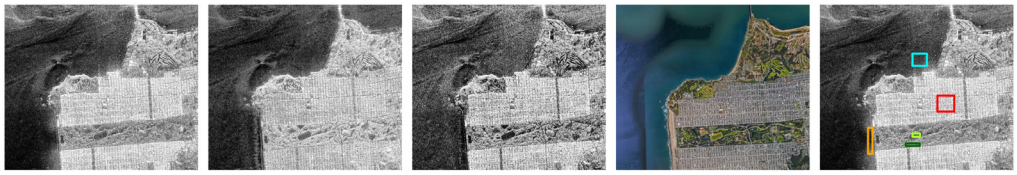

Fig. 9 Original actual PolSAR image. (a) HH polarization. (b) HV polarization. (c) VV polarization. (d) Same region obtained by Google Earth. (e) Reference areas: beach (orange), pasture (light green), urban zone (red), forest (dark green), and water (cyan).

4.2.2 *PolSAR images*

Figure 9 shows a fully polarimetric AIRSAR L-band image from San Francisco Bay, California, central latitude: 37°46′42″N, central longitude: 122°27′12″W, which is freely available in Ref. 34. Polarizations HH, HV, and VV are shown in Figs. 9(a)–9(c), respectively. The image size is 645×550 and the equivalent number of looks is $L = 2$. Figure 9(d) shows an optical image of the corresponding region taken from Google Earth. To test the feasibility of our classifier as a general-purpose method, we applied the SVM_A classifier previously trained with synthetic images as shown in the previous section. We have three classes, labeled according to the degree of texture, namely high (red), middle (green), and low (blue). The resulting classification performed separately on each band is shown in Fig. 10. It can be noticed that regions with high and intermediate degrees of texture are well recognized in HH polarization. Low texture zones are almost perfectly identified in HV polarization, while intermediate and high texture areas have high mutual confusion. Finally, the mutual confusion is higher for intermediate and low texture levels in VV polarization.

To assess the performance of the proposed approach, we retrained the model using the training reference areas marked in Fig. 9(d), consisting of the following zones: beach (orange, 1408 pixel), pasture (light green, 312 pixel), urban zone (red, 3021 pixel), forest (dark green, 470 pixel), and water (cyan, 2058 pixel). The classification was performed using the retrained SVM_A model in each band individually. In addition, a fusion procedure is applied by training the SVM classifier with the feature space formed by the feature sets A attained from the bands HH, HV, and VV, obtaining a feature vector of dimension twelve.

Due to the small sample size of some reference areas, we use the whole reference data for the training–validation–test procedure, since typical data augmentation procedures such as rotation or mirroring would not be adequate with the features used by this model. The mean and standard deviation achieved by the classifier are shown in Table 7, from which we select the following best models:

- HH polarization: radial kernel, $c = 10$ and $g = 2$.
- HV polarization: linear kernel, $c = 10$.
- VV polarization: radial kernel, $c = 10$ and $g = 1.5$.
- Polarization fusion: linear kernel, $c = 10$.

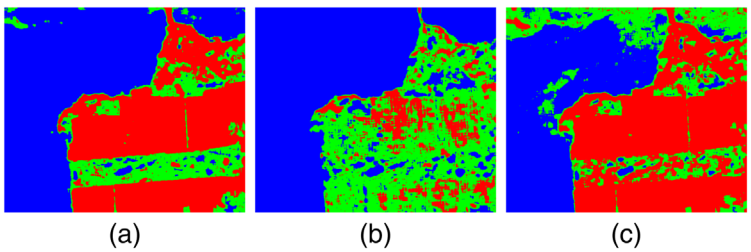

Fig. 10 Results of applying SVM_A to the images of Fig. 9, training the model with synthetic data ($L = 2$). High, medium, and low roughnesses are represented in red, green, and blue, respectively. (a) HH polarization, (b) HV polarization, and (c) VV polarization.

Table 7 Performance assessment for SVM_A method applied to the image of Fig. 9 according to each polarization.

Ker	Parameters	*F*1 Mean	*F*1 SD	IoU mean	IoU SD	AUC mean	AUC SD	Accuracy
(a) HH polarization								
L	$c = 5$	0.7651	0.0401	0.6811	0.0271	**0.8533**	0.0095	0.8721
P	$c = 1$, $d = 3$	0.8022	0.0070	0.7088	**0.0072**	0.8481	**0.0086**	0.8645
R	$c = 10$, $g = 2$	**0.8201**	0.0136	**0.7273**	0.0141	0.8493	0.0109	**0.8858**
S	$c = 10$, $g = 0.01$	0.6875	**0.0060**	0.6238	0.0092	0.8297	0.0152	0.8611
(b) HV polarization								
L	$c = 10$	**0.8756**	0.0208	**0.7922**	0.0296	**0.9379**	0.0125	0.9182
P	$c = 10$, $d = 3$	0.8750	0.0154	0.7908	0.0234	0.9346	0.0130	**0.9223**
R	$c = 10$, $g = 1$	0.8725	**0.0112**	0.7889	0.0187	0.9374	**0.0090**	**0.9223**
S	$c = 10$, $g = 0.01$	0.6547	0.0116	0.5612	**0.0144**	0.8464	0.0229	0.8631
(c) HV polarization								
L	$c = 5$	0.7935	0.0214	0.7494	0.0187	**0.9734**	0.0072	0.9512
P	$c = 10$, $d = 3$	0.8573	0.0201	0.7944	0.0214	0.9592	0.0091	0.9457
R	$c = 10$, $g = 1.5$	**0.8610**	0.0123	**0.7999**	**0.0119**	0.9606	**0.0070**	**0.9580**
S	$c = 10$, $g = 0.01$	0.7506	**0.0103**	0.7099	0.0171	0.9553	0.0182	0.9367
(d) Polarization fusion								
L	$c = 10$	**0.9915**	**0.0027**	**0.9834**	**0.0050**	**0.9975**	**0.0011**	**0.9959**
P	$c = 0.01$, $d = 3$	0.9870	0.0065	0.9750	0.0122	0.9931	0.0015	0.8274
R	$c = 10$, $g = 0.1$	0.9899	0.0058	0.9805	0.0109	0.9956	0.0024	0.9959
S	$c = 10$, $g = 0.01$	0.9395	0.0175	0.8966	0.0239	0.9756	0.0038	0.9704

Note: The bold type is used to show the best results.

The confusion matrix for the evaluation of the proposed method is shown in Table 8, considering three polarizations. Moreover, a comparative chart with the performance of different classifiers in terms of accuracy per class is shown in Table 9.

Figures 11(a)–11(c) show the results of applying the proposed classification method to the first three images of Fig. 9. Figure 11(d) shows the image classification when the variables of each band are joint to build the feature space. Figures 11(e)–11(g) show the results of applying the following sequence of algorithms: (1) the proposed classification method, (2) the majority filter, for HH, HV, and VV bands, respectively. Finally, Fig. 11(h) shows the image classification using all the features of every band altogether and then the majority filter. The image classification using SNAP tools for a similar procedure (without filtering) is shown in Fig. 12.

5 Discussion

The aim of this work is to assess the performance of the proposed model when it is applied to any type of area, location, or image format. For this reason, we used both synthetic images with different generation parameters and actual images with a diversity of modalities and locations. The different groups of experiments showed more than satisfactory results. With the synthetic images (Sec. 4.1.1), in the confusion matrices shown in Table 2, we can notice that in the low

Table 8 Confusion matrix for SVM_A method in different polarizations.

	Reference				
Prediction	Beach	Forest	Pasture	Urban zone	Water
(a) HH polarization					
Beach	61.43	0.00	32.76	0.00	7.21
Forest	0.00	98.91	1.72	0.00	0.00
Pasture	5.36	1.09	53.45	0.00	0.25
Urban zone	0.00	0.00	0.00	100.00	0.00
Water	33.21	0.00	12.07	0.00	92.54
(b) HV polarization					
Beach	87.14	0.00	10.34	0.00	4.73
Forest	0.00	65.22	0.00	4.02	0.00
Pasture	3.57	0.00	89.66	0.00	0.25
Urban zone	0.00	34.78	0.00	95.98	0.00
Water	9.29	0.00	0.00	0.00	95.02
(c) VV polarization					
Beach	92.86	0.00	48.28	0.00	0.75
Forest	0.00	96.74	0.00	0.80	0.00
Pasture	3.21	0.00	48.28	0.00	0.00
Urban zone	0.00	3.26	0.00	99.20	0.00
Water	3.93	0.00	3.45	0.00	99.25
(d) Polarization fusion					
Beach	98.57	0.00	3.45	0.00	0.00
Forest	0.00	100.00	0.00	0.00	0.00
Pasture	1.07	0.00	96.55	0.00	0.00
Urban zone	0.00	0.00	0.00	100.00	0.00
Water	0.36	0.00	0.00	0.00	100.00

texture zone both methods, SVM_{A^*} and SVM_A, almost completely coincide. For highly textured areas, including $\hat{\alpha}$ as a feature, produce considerable better results in the singlelook case. On the opposite side, and independently of the roughness, if $L = 2$, predictions are better if this parameter estimation is discarded. In the cases of noise contaminated data presented in Sec. 4.1.2, it can be observed that the best results are achieved by SVM_A, except for the first type of contamination in singlelook case. The accuracy decreases if the data are contaminated with type-III noise, especially for high values of k. On the other hand, the model has much better behavior for type-I and -II noise contamination.

The proposed feature set also behaves well with actual spaceborne SAR images. We compared our results with classifiers available in the SNAP Toolbox. The quality is at least equivalent or it behaves better especially in areas with high and intermediate roughness (even when we apply a pretrained classifier instead of retraining a new one for the images at hand). From the study of the image considered in Sec. 4.2.1, it can be observed that pasture region is classified

Table 9 Comparison of different classifiers applied to the images from Figs. 9(a)–9(c), in terms of accuracy values per class (in percentage).

Classifier	Beach	Forest	Pasture	Urban zone	Water
(a) HH polarization					
Our proposal SVM_A	70.24	**99.79**	59.62	**100.00**	**94.31**
RF	74.31	92.62	91.71	88.94	73.59
KD	72.84	94.57	**93.77**	90.56	72.36
ML	**78.19**	77.56	86.92	77.28	73.71
MD	72.96	76.72	87.07	75.73	72.36
(b) HV polarization					
Our proposal SVM_A	**88.92**	65.32	88.46	**96.13**	**96.60**
RF	75.22	92.94	92.19	91.12	75.73
KD	76.41	**94.96**	**93.14**	93.50	77.68
ML	76.88	69.83	89.85	65.82	77.24
MD	73.12	84.38	78.95	72.09	75.38
(c) VV polarization					
Our proposal SVM_A	**94.18**	**97.02**	51.28	**99.64**	**99.42**
RF	81.96	93.10	91.55	82.55	71.85
KD	83.39	95.04	**93.70**	84.42	74.07
ML	79.14	75.06	71.41	70.86	74.19
MD	85.41	78.35	85.77	74.23	73.79
(d) Polarization fusion					
Our proposal SVM_A	**99.64**	**100.00**	**96.79**	**100.00**	**100.00**
RF	85.77	94.85	93.66	94.13	88.54
KD	85.80	94.33	94.13	93.77	88.10
ML	79.14	77.95	91.36	77.24	80.89
MD	82.87	83.35	88.38	74.27	79.14

Note: The bold type is used to show the best results.

with the highest accuracy, followed by urban and forest zones. Water bodies are adequately detected, although about 20% of the freshwater region (lagoon) has mutual confusion with sea. This can be attributed to the fact that textures in these water surfaces mostly depend on the wind condition, which in close regions is going to be similar, notwithstanding if it is a freshwater body or sea near the shoreline. A better differentiation could be achieved taking a sea training region much farther from the shoreline. Also, there is nearly 23% of confusion among forest and urban areas. This can be attributed to the fact that this is a small town located in previously forested and pinewood zones, with very few tall buildings and a high amount of trees in the streets.

Finally, from the image analyzed in Sec. 4.2.2, it can be observed that the accuracy improves significantly when we fuse together the information from the three bands, reaching a value of 99.59%. If we analyze only one band, VV has the best behavior with accuracy of 95.80%. Regarding the reference area, notice that the identification of urban and forest zones is near optimal in the HH polarization. Also all other regions except pasture are well identified in

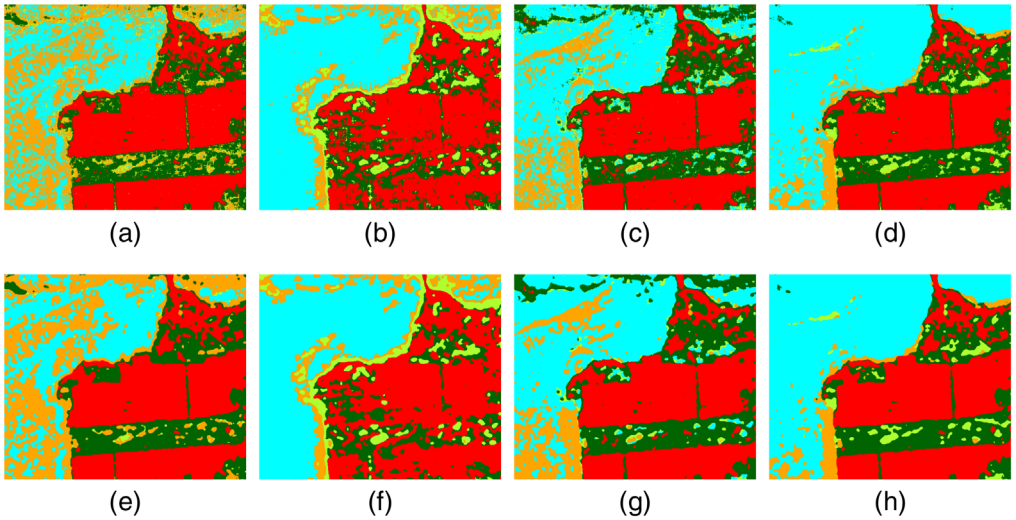

Fig. 11 Results of applying the classification method to the image from Fig. 9 and the majority filter. (a) HH before majority filter. (b) HV before majority filter. (c) VV before majority filter. (d) All bands before majority filter. (e) HH post majority filter. (f) HV post majority filter. (g) VV post majority filter. (h) All bands post majority filter.

VV polarization. The accuracy of the method in pasture recognition is strongly better in HV rather than the other polarizations. It can be appreciated that the five area types are well classified when we use together the features of the three polarizations, especially after applying the majority filter which improves the results eliminating small misclassifications. There is no ground truth available for this image, and the interpretation of this kind of images is known to be difficult.[35] However, our results are consistent with a visual inspection over the optical image.

6 Conclusions and Future Work

We presented a new approach for monopolarimetric and polarimetric SAR image classification using a vector of local features and the SVM method. Our main contribution is a feasible region discrimination performed by means of a texture feature vector containing Tsallis entropy, optimal entropic index, and FD estimations. The introduction of such a vector of descriptors to represent regions with different degrees of texture is based on the idea that the combination of several image characteristics provides more information than each one separately. In addition, we propose a method to classify PolSAR images as the fusion of the feature vectors obtained per band, which produces a much more accurate image classification. The performance of the methods is assessed using the accuracy value, confusion matrices, $F1$-score, IoU, and AUC.

Experimental results in actual images of this sort show that the proposed classification technique achieves significant accuracy values. As is widely acknowledged, speckle noise hinders a correct interpretation of SAR images, in particular where region segmentation depends on adequate texture descriptors. There exists a vast literature focused on speckle reduction filters, whose application facilitates general-purpose automated region segmentation, at the expense of hampering the original texture information. For region identification (which is the aim of our proposal), the goal is to provide adequate textural features, and if possible link them to semantic or object-based information. In this way, further analysis tasks can be facilitated relating them to the specific application context. In this purpose, our contribution provides better performance as compared with of-the-shelf library functionalities, for example, the ones provided by the SNAP suite. As future work, we are interested in the computation of Tsallis entropy formula for the $\mathcal{G}_I^0$ distribution with the aim of using it as a theoretical texture feature.

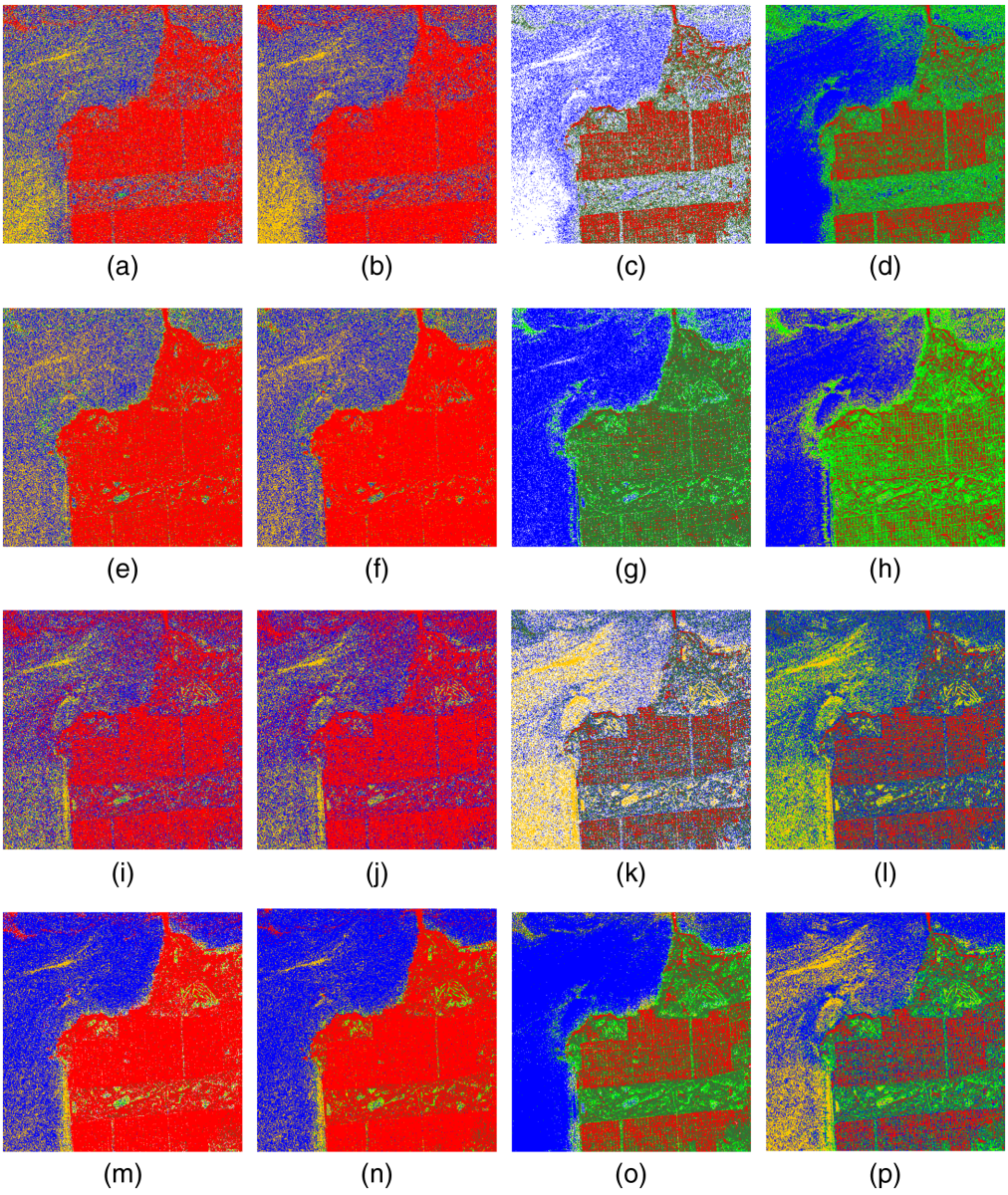

Fig. 12 Results of applying different classifiers from SNAP tools to the image of Fig. 9. (a) RF to HH polarization. (b) KD to HH polarization. (c) ML to HH polarization. (d) MD to HH polarization. (e) RF to HV polarization. (f) KD to HV polarization. (g) ML to HV polarization. (h) MD to HV polarization. (i) RF to VV polarization. (j) KD to VV polarization. (k) ML to VV polarization. (l) MD to VV polarization. (m) RF to polarization fusion. (n) KD to polarization fusion. (o) ML to polarization fusion. (p) MD to polarization fusion.

7 Appendix A: Specifications

Simulations were performed using the R language and environment for statistical computing version 3.6.3,[36] in a computer with processor Intel© Core™, i7-6700K CPU 3.40 GHz 3.41 GHz, 16 GB RAM, System Type 64 bit operating system.

Acknowledgments

This work was partially supported by the Universidad Tecnológica Nacional Grant Nos. PID ASUTNBA0005149, PGI 24/K083 from SGCyT-UNS, and PICT 2018-4137 from ANPCyT. The authors declare that they do not have conflicts of interest.

References

1. J. Lee and E. Pottier, *Polarimetric Radar Imaging: From Basic to Application*, CRC Press, Boca Raton, FL (2011).
2. C. Oliver and S. Quegan, *Understanding Synthetic Aperture Radar Images*, Artech House, Boston (1998).
3. D.-X. Yue et al., "SAR image statistical modeling Part I: single-pixel statistical models," *IEEE Geosci. Remote Sens. Mag.* **9**(1), 82–114 (2021).
4. D.-X. Yue et al., "SAR image statistical modeling Part II: spatial correlation models and simulation," *IEEE Geosci. Remote Sens. Mag.* **9**(1), 115–138 (2021).
5. A. Frery et al., "A model for extremely heterogeneous clutter," *IEEE Trans. Geosci. Remote Sens.* **35**(3), 648–659 (1997).
6. J. Gambini et al., "SAR images segmentation through B-spline deformable contours and fractal dimension," International Society for Photogrammetry and Remote Sensing, Istanbul, Turkey, 2004, https://www.cartesia.org/geodoc/isprs2004/comm3/papers/441.pdf.
7. D. Riccio et al., "Fractal dimension images from SAR images," in *IEEE Int. Conf. Image Process.*, pp. 106–110 (2014).
8. K. Falconer, *Fractal Geometry: Mathematical Foundations and Applications*, John Wiley & Sons, Chichester, England (1990).
9. K. Clarke, "Computation of the fractal dimension of topographic surfaces using the triangular prism surface area method," *Comput. Geosci.* **12**(5), 713–722 (1986).
10. A. Nascimento, R. Cintra, and A. Frery, "Hypothesis testing in speckled data with stochastic distances," *IEEE Trans. Geosci. Remote Sens.* **48**(1), 373–385 (2010).
11. A. L. Barbieri et al., "An entropy-based approach to automatic image segmentation of satellite images," *Physica A* **390**, 512–518 (2011).
12. C. Tsallis, "Possible generalization of Boltzmann–Gibbs statistics," *J. Stat. Phys.* **52**(1), 479–487 (1988).
13. C. E. Shannon, "A mathematical theory of communication," *Bell Syst. Tech. J.* **27**, 379–423 (1948).
14. A. C. Frery, R. J. Cintra, and A. D. C. Nascimento, "Entropy-based statistical analysis of PolSAR data," *IEEE Trans. Geosci. Remote Sens.* **51**(6), 3733–3743 (2013).
15. B. E. Boser, I. M. Guyon, and V. N. Vapnik, "A training algorithm for optimal margin classifiers," in *Proc. Fifth Annu. Workshop Comput. Learn. Theory*, Association for Computing Machinery, New York, NY, pp. 144–152 (1992).
16. C. Lanying, "Classification SAR targets with support vector machine," *Proc. SPIE* **6497**, 219–228 (2007).
17. A. Zhang et al., "Region level SAR image classification using deep features and spatial constraints," *ISPRS J. Photogramm. Remote Sens.* **163**, 36–48 (2020).
18. Y. Wu et al., "High-resolution synthetic aperture radar image classification using multi-scale anisotropic convolutional sparse coding," *J. Appl. Remote Sens.* **15**(1), 016515 (2021).
19. P. Simon and V. Uma, "Review of texture descriptors for texture classification," in *Data Engineering and Intelligent Computing*, S. C. Satapathy et al., Eds., pp. 159–176, Springer, Singapore (2018).
20. P. Cavalin and L. S. Oliveira, "A review of texture classification methods and databases," in *30th SIBGRAPI Conf. Graphics, Patterns and Images Tutorials*, pp. 1–8 (2017).
21. M. Mejail et al., "Classification of SAR images using a general and tractable multiplicative model," *Int. J. Remote Sens.* **24**(18), 3565–3582 (2003).
22. C. Broyden, "A class of methods for solving nonlinear simultaneous equations," *Math. Comput.* **19**, 577–593 (1965).
23. A. Frery, F. Cribari-Neto, and M. de Souza, "Analysis of minute features in speckled imagery with maximum likelihood estimation," *EURASIP J. Adv. Signal Process.* **2004**(16), 370–375 (2004).
24. B. B. Mandelbrot and J. W. V. Ness, "Fractional Brownian motions, fractional noises and applications," *SIAM Rev.* **10**(4), 422–437 (1968).
25. A. F. Silvetti and C. A. Delrieux, "Quadratic self-correlation: an improved method for computing local fractal dimension in remote sensing imagery," *Comput. Geosci.* **60**, 142–155 (2013).

26. C. Tsallis, "Entropic nonextensivity: a possible measure of complexity," *Chaos Solitons Fractals* **13**, 371–391 (2002).
27. A. Ramrez-Reyes et al., "Determining the entropic index q of Tsallis entropy in images through redundancy," *Entropy (Basel)* **18**(8), 299–313 (2016).
28. G. James et al., *An Introduction to Statistical Learning: With Applications in R*, Springer, New York (2013).
29. D. Chan et al., "Sampling from the $\mathcal{G}_I^0$ distribution," *Monte Carlo Methods Appl.* **24**, 271–287 (2018).
30. A. Frery, S. Ferrero, and O. H. Bustos, "The influence of training errors, context and number of bands in the accuracy of image classification," *Int. J. Remote Sens.* **30**(6), 1425–1440 (2009).
31. J. Gambini et al., "Parameter estimation in SAR imagery using stochastic distances and asymmetric kernels," *IEEE J. Sel. Top. Appl. Earth Obs. Remote Sens.* **8**(1), 365–375 (2015).
32. Sentinel application platform (SNAP) - European Space Agency (ESA), "Sentinel application platform," v8.0.8, http://step.esa.int/main/toolboxes/snap/ (accessed 23 December 2021).
33. Comisión Nacional de Actividades Espaciales (CONAE), "SAOCOM catalogue," https://catalog.saocom.conae.gov.ar/catalog/ (accessed 23 December 2021).
34. European Space Agency (ESA), "PolSARpro v6.0 (Biomass Edition) Toolbox," https://earth.esa.int/web/polsarpro/data-sources/sample-datasets (accessed 23 December 2021).
35. M. Ahishali et al., "Classification of polarimetric SAR images using compact convolutional neural networks," *GISci. Remote Sens.* **58**(1), 28–47 (2021).
36. R Core Team, "R: a language and environment for statistical computing," R Foundation for Statistical Computing, Vienna, Austria, 2016, https://www.R-project.org/.

Andrea Rey received her PhD in mathematics from the Universidad de Buenos Aires (UBA), Argentina. She works at the Universidad Tecnológica Nacional Facultad Regional Buenos Aires as a professor and has several years of experience in teaching and research. She is a member of the Centro de Procesamiento de Seales e Imágenes (UTN-FRBA). She has research publications in international journals and conferences. Her research interests include data mining, machine learning, as well as image and signal analysis.

Juliana Gambini is a professor at the University Intituto Tecnológico de Buenos Aires and Universidad Nacional de Tres Febrero, Argentina. She received her BS degree in mathematics and her PhD in computer science both from the UBA, Buenos Aires, Argentina, in 1996 and 2006, respectively. Her current research interests include SAR image processing, statistical learning, and image recognition.

Claudio Delrieux is a PhD in computer science from the Universidad Nacional del Sur (Argentina) and Fulbright posdoctoral fellow from the University of Denver. He is full professor and PI at the Electric and Computer Engineering Department in the Universidad Nacional del Sur (Argentina), fellow of the National Council of Science and Technology of Argentina (CONICET), and chair of the Imaging Sciences Laboratory. His current interests are image and video processing, computer graphics, scientific visualization, and artificial intelligence.